

Lamp mapping technique for independent determination of the water vapor mixing ratio calibration factor for a Raman lidar system

Demetrius D. Venable,^{1,*} David N. Whiteman,² Monique N. Calhoun,¹
Afusat O. Dirisu,² Rasheen M. Connell,¹ and Eduardo Landulfo³

¹Department of Physics and Astronomy, Howard University, Washington, D.C. 20059, USA

²NASA Goddard Space Flight Center, Greenbelt, Maryland 20771, USA

³Centro de Lasers e Aplicacoes, Instituto de Pesquisas Energeticas e Nucleares, Sao Paulo, Brazil

*Corresponding author: dvenable@howard.edu

Received 15 December 2010; accepted 21 March 2011;
posted 3 June 2011 (Doc. ID 139712); published 5 August 2011

We have investigated a technique that allows for the independent determination of the water vapor mixing ratio calibration factor for a Raman lidar system. This technique utilizes a procedure whereby a light source of known spectral characteristics is scanned across the aperture of the lidar system's telescope and the overall optical efficiency of the system is determined. Direct analysis of the temperature-dependent differential scattering cross sections for vibration and vibration-rotation transitions (convolved with narrowband filters) along with the measured efficiency of the system, leads to a theoretical determination of the water vapor mixing ratio calibration factor. A calibration factor was also obtained experimentally from lidar measurements and radiosonde data. A comparison of the theoretical and experimentally determined values agrees within 5%. We report on the sensitivity of the water vapor mixing ratio calibration factor to uncertainties in parameters that characterize the narrowband transmission filters, the temperature-dependent differential scattering cross section, and the variability of the system efficiency ratios as the lamp is scanned across the aperture of the telescope used in the Howard University Raman Lidar system. © 2011 Optical Society of America

OCIS codes: 010.1280, 280.3640.

1. Introduction

Several articles concerning the use of standard lamps for calibration of a Raman lidar water vapor system have been reported. Sherlock *et al.* [1] reported on a methodology for independent calibration using diffuse sunlight and a stationary xenon arc lamp, both of which were shown to pose difficulties in their use. Leblanc and McDermid [2] reported on the use of a hybrid technique utilizing a stationary calibration lamp in conjunction with radiosondes.

Whiteman *et al.* [3] discussed the advantages of using a scanning lamp system over a stationary lamp as well as failure modes for both the stationary and scanning-mode techniques. Also, Sobral-Torres *et al.* [4] and Landulfo *et al.* [5] reported on a calibration system with wide (~20 nm) bandpass filters utilizing a scanning lamp configuration. In this paper we expand the mapping technique described by Landulfo *et al.* for wide bandpass filters [5] to the case of narrowband filters (~0.3 nm or smaller) where the temperature dependence of the differential scattering cross sections must be taken into consideration.

The mapping experiment involves scanning a lamp with known spectra irradiance over the aperture of

the lidar's system telescope. Data are collected at each lamp position (or data cell). This paper describes the appropriate analysis to determine the water vapor mixing ratio calibration factor from these data. The technique was applied to the Raman lidar system based at Howard University's Beltsville, Maryland, campus, and an independent determination of the water vapor mixing ratio calibration constant was obtained for this system. The Howard University Raman Lidar (HURL) is a fiber-coupled three-channel system that detects backscattered light near the excitation wavelength and inelastic Raman signals from nitrogen and water vapor molecules [6]. The system utilizes an Nd:YAG laser operating at the third harmonic (354.7 nm). The corresponding vibrational transitions for nitrogen and water vapor occur at 386.7 nm and 407.5 nm, respectively. Narrowband interference filters with FWHM bandpass values of ~0.25–0.30 nm are used. Detailed discussions of the HURL system [6] and of water vapor measurements made with the system as it was configured during 2006 measurement campaigns [7] have been given.

This current paper is based on the same configuration reported earlier [7] but with the system components (such as photomultiplier tubes and interference filters) used during the September 2009 through August 2010 measurement campaigns. Technical details of the calibration factor and mapping technique are discussed in the next section, followed by detailed discussions on the sensitivity of the calibration technique to uncertainties in calculations of temperature-dependent cross sections, the uncertainties in the measurements of the filter parameters, and the variability of the system efficiency ratios across the face of the telescope.

2. Technical Background

The temperature-dependent lidar equation for Raman scattering is [8]

$$P(\lambda, z) = q_X P_L(\lambda_L) O_X(z) \frac{A c \tau}{z^2 2} N_X(z) F_X(T) \frac{d\sigma_X(\pi)}{d\Omega} \xi(\lambda) \times \exp \left[- \int_0^z [\alpha(\lambda_L, z') + \alpha(\lambda, z')] dz' \right] + q_X B(\lambda). \quad (1)$$

Here P is the measured returned signal; λ is the wavelength; P_L is the laser power; O is the overlap function; A is the area of the telescope; c is the speed of light; τ is the laser pulse duration; N is the total number density of scatterers; $d\sigma(\pi)/d\Omega$ is the Raman differential cross section in the backscatter direction due to excitation at the laser wavelength λ_L ; α is the extinction coefficient; B is the background power; z is the altitude; T is the temperature (K); ξ is the overall system optical efficiency; q is a proportionality factor that converts the detected optical signal into the measured electrical signal; and X represents either L for the 355 channel (backscatter at laser wave-

length), N for the nitrogen channel, or H for the water vapor channel. The factor $F(T)$ contains the temperature dependence for the Raman lidar equation and is given by [8]

$$F_X(T) \equiv \frac{\int_{\Delta\lambda_X} \frac{d\sigma_X(\lambda, T, \pi)}{d\Omega} \xi(\lambda) d\lambda}{\frac{d\sigma_X(\pi)}{d\Omega} \xi(\lambda_X)}, \quad (2)$$

where $d\sigma/d\Omega(\lambda, T, \pi)$ is the temperature-dependent Raman differential cross section and $\Delta\lambda_X$ represents the bandpass over which the Raman signal is detected for either nitrogen ($X \rightarrow N$) or water vapor ($X \rightarrow H$).

The overall system optical efficiency term is expressed as

$$\xi(\lambda) = \varepsilon(\lambda)\kappa(\lambda), \quad (3)$$

where the factor $\varepsilon(\lambda)$ is the interference filter transmission efficiency at wavelength λ , and the factor $\kappa(\lambda)$, assumed to be constant over the bandpass of the interference filter, represents all other system efficiencies. In this paper, we refer to $\kappa(\lambda)$ as the system efficiency and $\varepsilon(\lambda)$ as the filter efficiency. In the case of $\lambda = \lambda_X$, $\xi(\lambda)$ gives the overall system efficiency at the characteristic wavelength for channel X . If the interference filter peak transmission is centered on λ_X , then the peak value of $\xi(\lambda)$ in the vicinity of λ_X is at λ_X .

The water vapor mixing ratio, $w(z)$, defined as the ratio of the mass of water vapor (mass_H) at altitude z to the mass of dry air ($\text{mass}_{\text{dryair}}$) at that altitude can be expressed as

$$w(z) \equiv \frac{\text{mass}_H}{\text{mass}_{\text{dryair}}} = \frac{N_H(z)M_H}{N_{\text{dryair}}(z)M_{\text{dryair}}} \approx 0.7808 \frac{M_H}{M_{\text{dryair}}} \left(\frac{N_H(z)}{N_N(z)} \right), \quad (4)$$

where M_H is the molecular weight of water vapor (~18.02 g/mol), M_{dryair} is the molecular weight of dry air (~28.97 g/mol), and $N_N(z) \approx 0.7808 N_{\text{dryair}}(z)$. Solving Eq. (1) for $N_X(z)$ leads to the ratio $N_H(z)/N_N(z)$; hence $w(z)$ can be written as

$$w(z) \approx 0.486 \frac{q_N \kappa(\lambda_N) F_N(T) \frac{d\sigma_N(\pi)}{d\Omega} \varepsilon(\lambda_N) P(\lambda_H, z) O_N(z)}{q_H \kappa(\lambda_H) F_H(T) \frac{d\sigma_H(\pi)}{d\Omega} \varepsilon(\lambda_H) P(\lambda_N, z) O_H(z)} \times \Delta\tau(\lambda_N, \lambda_H, z), \quad (5)$$

where

$$P(\lambda_X, z) = P(\lambda_X, z) - q_X B(\lambda_X) \quad (6)$$

is the background subtracted lidar signal, and

$$\Delta\tau(\lambda_N, \lambda_H, z) \equiv \exp\left[-\int_0^z [\alpha(\lambda_N, z') - \alpha(\lambda_H, z')] dz'\right] \quad (7)$$

is the differential transmission factor.

Normally, $F(T)$ is applied as a correction to the raw lidar data, i.e., $P(\lambda_X, z)$. Then the water vapor mixing ratio calibration factor, C_R , is defined as a temperature-independent term and is given by

$$C_R \cong 0.486 \frac{q_N \kappa(\lambda_N) \frac{d\sigma_N(\pi)}{d\Omega} \varepsilon(\lambda_N)}{q_H \kappa(\lambda_H) \frac{d\sigma_H(\pi)}{d\Omega} \varepsilon(\lambda_H)}. \quad (8)$$

If, on the other hand, one wishes to investigate the behavior of the water vapor mixing ratio calibration factor when the temperature corrections are ignored, an alternative form of the water vapor mixing ratio calibration factor, $C'_R(T)$, that includes the temperature-dependent term must be defined as

$$\begin{aligned} C'_R(T) &\cong 0.486 \frac{q_N \kappa(\lambda_N) F_N(T) \frac{d\sigma_N(\pi)}{d\Omega} \varepsilon(\lambda_N)}{q_H \kappa(\lambda_H) F_H(T) \frac{d\sigma_H(\pi)}{d\Omega} \varepsilon(\lambda_H)} \\ &\cong 0.486 \frac{q_N \kappa(\lambda_N) \langle \sigma_N | \varepsilon_N \rangle}{q_H \kappa(\lambda_H) \langle \sigma_H | \varepsilon_H \rangle}. \end{aligned} \quad (9)$$

Here we have introduced the shorthand notation $\langle \sigma_X | \varepsilon_X \rangle$ to represent the integral in Eq. (2), which we define as the convolved cross section, i.e.,

$$\begin{aligned} \langle \sigma_X | \varepsilon_X \rangle &\equiv \int_{\Delta\lambda_X} \frac{d\sigma_X(\lambda, T, \pi)}{d\Omega} \varepsilon(\lambda) d\lambda \\ &= F_X(T) \frac{d\sigma_X(\pi)}{d\Omega} \varepsilon(\lambda_X). \end{aligned} \quad (10)$$

Because the individual Raman transition lines are much narrower than the filter function, a summation over individual transitions as defined by Eq. (11) can be used. This approach ignores any information concerning the shapes of the Raman transition lines. Thus, in practice we use a summation over discrete spectral states to approximate the integral. That is,

$$\int_{\Delta\lambda_X} \frac{d\sigma_X(\lambda, T, \pi)}{d\Omega} \varepsilon(\lambda) d\lambda \rightarrow \sum_i \left\{ \frac{d\sigma_X(\lambda_i, T, \pi)}{d\Omega} \varepsilon(\lambda_i) \right\}. \quad (11)$$

In the conversion from an integral to a summation, a term $\Delta\lambda_i$ would generally be used; however, the differential cross section values $d\sigma_X(\lambda_i, T, \pi)/d\Omega$ that are used in this paper were calculated using the data from Avila *et al.* [9] and are in units of m^2/sr . Thus, in practice all that is needed is to sum up these values as indicated on the right-hand side of Eq. (11).

As shown in Eq. (12), $S_{X,i}^{\text{out}}$ is the measured output of the mapping experiment at a single cell location for channel X . Functionally, $S_{X,i}^{\text{out}}$ is the measured output signal in the i th cell and is given by the convolution of the system efficiency and the lamp intensity,

$I^{\text{in}}(\lambda)$, as depicted in Fig. 1. Note that the integral is now taken over the range $\Delta\lambda_{\text{filter}}$ since, in practice, the transmission characteristics of the filter define the useful limits of the integral:

$$\begin{aligned} S_{X,i}^{\text{out}} &= q_X \int_{\Delta\lambda_{\text{filter}X}} \xi_{X,i}(\lambda) I^{\text{in}}(\lambda) d\lambda \\ &= q_X \kappa_i(\lambda_X) \int_{\Delta\lambda_{\text{filter}X}} \varepsilon_{X,i}(\lambda) I^{\text{in}}(\lambda) d\lambda. \end{aligned} \quad (12)$$

The ratio of these measurements is defined by the notation $S_{HN,i}^{\text{out}} \equiv S_{H,i}^{\text{out}}/S_{N,i}^{\text{out}}$. In practice, what is desired is an averaged value of $S_{HN,i}^{\text{out}}$ for all cells. This averaged quantity would represent all measurements taken across the entire aperture of the telescope and is given in Eq. (13),

$$S_{HN}^{\text{out}} = \frac{1}{n} \sum_{i=1}^n S_{HN,i}^{\text{out}} = \frac{1}{n} \sum_{i=1}^n S_{H,i}^{\text{out}}/S_{N,i}^{\text{out}}, \quad (13)$$

where n is the number of cells measured across the telescope aperture. Typically, we measure about 200 cells per scan. The advantage of making measurements at multiple locations across the aperture as opposed to making a measurement at a single location has been discussed elsewhere [3]. In the right-most term of Eq. (12), Eq. (3) has been used to write the overall system efficiency, $\xi(\lambda)$, as the product of $\varepsilon(\lambda)$ and $\kappa(\lambda)$. The limits for the integral are selected so as to perform the integration over the bandpass of the filter. For simplicity, the right-most integral in Eq. (12) is defined as $S_{X,i}^{\text{in}}$ and is given by

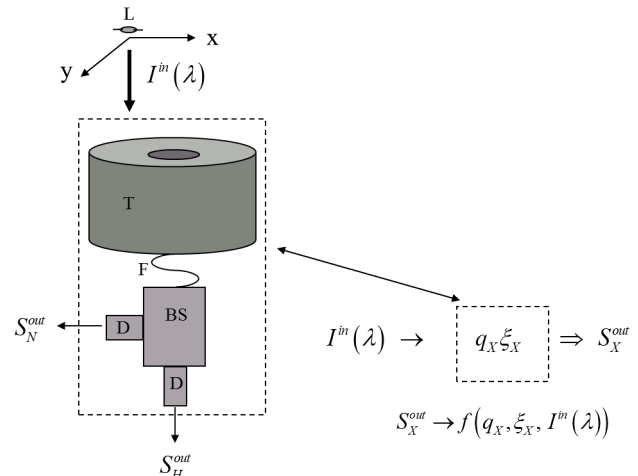


Fig. 1. Schematic layout of the mapping setup. L, lamp; T, telescope; F, optical fiber; BS, wavelength separation unit (beam splitters, narrowband interference filters, collimating lenses, etc.); D, detector electronic components that convert the optical signals to measured electrical signals; S_H^{out} , water vapor channel signal; and S_N^{out} , nitrogen channel signal. The lamp (with intensity I^{in}) is scanned in the x - y plane across the telescope aperture. ξ is the overall optical efficiency of the system, and the factor q_X represents the conversion of the detected optical signal into the measured electrical signal. S_X^{out} is a function of the overall optical efficiency, the electrical efficiency, and the lamp intensity.

$$S_{X,i}^{\text{in}} = \int_{\Delta\lambda_{\text{filter}X}} \varepsilon_{X,i}(\lambda) I^{\text{in}}(\lambda) d\lambda = \frac{S_{X,i}^{\text{out}}}{q_X \kappa_i(\lambda_X)}. \quad (14)$$

Equation (14) represents the convolution of the spectral lamp intensity and the transmission of the interference filter. In general, however, the transmission efficiency of the interference filter is not known as a function of cell location, i . What is known is the average value of the transmission over the useful aperture of the filter. Therefore, in practice, what is calculated is the average value given in Eq. (14a).

$$S_{HN}^{\text{in}} = \frac{\int_{\Delta\lambda_{\text{filter}H}} \varepsilon_H(\lambda) I^{\text{in}}(\lambda) d\lambda}{\int_{\Delta\lambda_{\text{filter}N}} \varepsilon_N(\lambda) I^{\text{in}}(\lambda) d\lambda} = \frac{q_N \kappa(\lambda_N)}{q_H \kappa(\lambda_H)} S_{HN}^{\text{out}}. \quad (14a)$$

The ratio $\kappa(\lambda_N)/\kappa(\lambda_H)$ is then given by

$$\frac{\kappa(\lambda_N)}{\kappa(\lambda_H)} = \frac{q_H S_{HN}^{\text{in}}}{q_N S_{HN}^{\text{out}}}. \quad (15)$$

C_R now becomes

$$C_R \cong 0.486 \frac{S_{HN}^{\text{in}} \frac{d\sigma_N(\pi)}{d\Omega} \varepsilon(\lambda_N)}{S_{HN}^{\text{out}} \frac{d\sigma_H(\pi)}{d\Omega} \varepsilon(\lambda_H)}, \quad (16)$$

and $C'_R(T)$ becomes

$$C'_R(T) \cong 0.486 \frac{S_{HN}^{\text{in}}}{S_{HN}^{\text{out}}} \left[\frac{\langle \sigma_N | \varepsilon_N \rangle}{\langle \sigma_H | \varepsilon_H \rangle} \right]. \quad (17)$$

Equation (16) allows one to calculate the water vapor mixing ratio calibration factor using the results of the mapping experiment. Equation (17) allows an investigation of the temperature-dependent form of $C'_R(T)$ when the lidar data are not corrected for $F(T)$.

3. Discussion

In this section we briefly discuss the (1) lamp function, (2) filter functions, (3) convolved differential cross section terms, and (4) mapping experiment. These are followed by more detailed discussions of the (5) water vapor mixing ratio calibration factor, C_R , and (6) sensitivity of the temperature-dependent form of $C'_R(T)$ to the parameters of the interference filters.

A. Lamp Function

The light source used in the mapping experiment was a noncalibrated 200 W tungsten–halogen (OL220) lamp manufactured by Optronic Laboratories, USA [10]. The lamp was powered with the Optronic Laboratories OL 83A Programmable dc current source. Nine points (ordered pairs of lamp intensity versus wavelength) in the vicinity of the Raman transitions of interest were fitted to a Planck blackbody curve to provide an appropriate function that describes the behavior of the lamp in the region of interest (~ 340 – 420 nm). These points were obtained from the manufacturer's supplied documentation. The results are plotted in Fig. 2. Since this experiment in-

volves only the ratio of the signals in the water vapor and nitrogen channels, the important parameter is the relative output of the lamp at these wavelengths. To validate the accuracy in the relative values of the uncalibrated lamp's spectral irradiance, we compared a typical 200 W uncalibrated lamp (using irradiance data provided by the manufacturer) with a NIST traceable calibrated 1000 W tungsten–halogen lamp provided by the same manufacturer and found that the blackbody temperature (4143.63 K) obtained from the curve fit for the calibrated lamp was within 0.01 K of the blackbody temperature (4143.64 K) of a typical uncalibrated 200 W lamp. This is consistent with the manufacturer's experience that the uncalibrated lamp's color temperature should not vary by more than 20 K from a calibrated lamp [11]. The error for the lamp intensity ratio (for wavelengths of ~ 387 nm and ~ 408 nm) is estimated to be less than 0.3% [3]. The fitted Planck blackbody function for the 200 W lamp was used as the lamp output intensity, I^{in} , in the analyses of the integral in Eq. (12). This lamp provided a reasonable count rate of ~ 4 MHz in the nitrogen and water vapor channels for our system.

B. Filter Function

In order to determine the interference filter transmission functions that will be used in the evaluation of $\varepsilon(\lambda)$, the filter transmission curves provided by the manufacturer were digitized to obtain a discrete set of transmission-wavelength ordered pairs for each filter. Because the out-of-band blocking of the filters was specified to be better than 10^{-6} , these data were corrected to compensate for a baseline offset of several percentage points in the manufacturer-provided

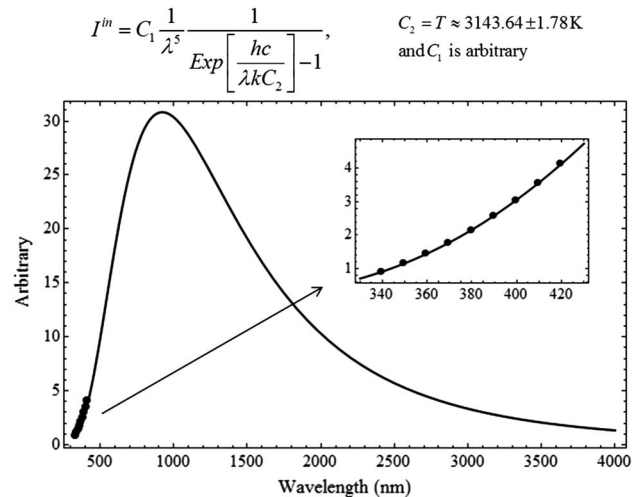
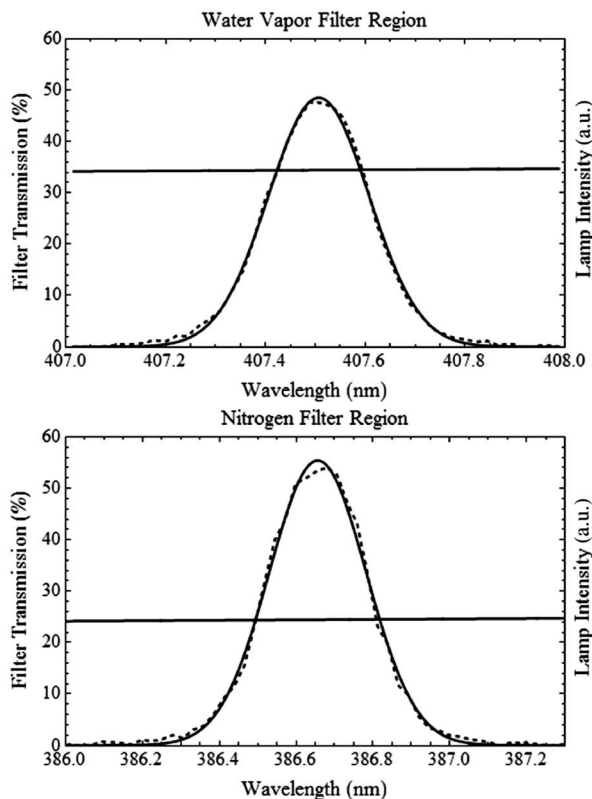


Fig. 2. Nonlinear least squares fit function obtained for the uncalibrated 200 W tungsten–halogen lamp near the excitation and Raman wavelengths for the HURL system. The fitting parameter, $C_2 = 3143.64 \pm 1.78$, corresponds to the blackbody temperature and is found to be in good agreement with a 1000 W NIST traceable same-color temperature-calibrated lamp. I^{in} , lamp intensity; h , Planck's constant; c , the speed of light; k , Boltzmann's constant; and λ , wavelength.

curves. A nonlinear curve-fitting method was then used to fit the baseline corrected data of each filter to a Gaussian function using the peak transmission, central wavelength, and FWHM as fitting parameters. The resulting Gaussian function obtained for each filter, $\mathcal{F}_{\text{Gauss}}(\lambda)$, was used in subsequent analyses where $\varepsilon(\lambda) \equiv \mathcal{F}_{\text{Gauss}}(\lambda)$. Figure 3 shows a comparison of the fitted function to the baseline corrected original data.

Once the lamp's Planck function and the filters' Gaussian functions are known, the average ratio S_{HN}^{in} may be obtained using the ratio of the integrals as given in Eqs. (14) and (14a). For our system, we obtain 0.984 ± 0.014 for this value. It is important to note that the accuracy of this ratio strongly depends on the accuracy to which the relative filter



$$\mathcal{F}_{\text{Gauss}} = C_1 \text{Exp} \left[-\frac{1}{2} \left(2\sqrt{2 \log_e [2]} \frac{x - C_2}{C_3} \right)^2 \right]$$

Filter	λ_0 (nm)	FWHM (nm)	Amplitude (%)
N	386.67	0.30	55.41
H	407.51	0.24	48.53

Fig. 3. Transmission curves for water vapor and nitrogen filters. Dotted lines, digitized curves provided by the after-baseline-offset corrections; solid curves, nonlinear least squares fit to Gaussian functions. C_1 , C_2 , and C_3 are the fitting parameters for the peak transmission (amplitude), center wavelength (λ_0), and FWHM of the corresponding Gaussian function, respectively. The solid nearly horizontal lines give the lamp function (in arbitrary units) in the vicinity of the bandpass of the respective filters.

transmissions are known. The error in the ratio is estimated by assuming that the error in the lamp intensity ratio is less than 0.3% as stated above. Furthermore, we assume an absolute error of 1% in the measured filter transmission at the water vapor and nitrogen Raman wavelengths. We estimate this to be an upper limit on the manufacturer's ability to specify the peak transmission of such filters. For comparison, we also calculated the ratio S_{HN}^{in} using an interpolation function of the baseline corrected digitized filter data rather than the Gaussian fit function. Values for the ratios for the two cases were within 0.2% of each other. Results presented in this paper are based on the use of the Gaussian fitting function to characterize the transmission filters.

C. Convolved Differential Cross Sections

The differential cross section of Raman scattering for both water vapor and nitrogen were obtained from analysis of the respective vibrational-rotational transitions in the region of interest. The transitions in the OH-stretch region for water vapor ($3630\text{--}3660\text{ cm}^{-1}$) were calculated using the methods described by Avila *et al.* [9], while for nitrogen, the transitions were calculated using the methods summarized in the article by Adam [12]. We obtained values for the total cross section of $2.744 \times 10^{-34}\text{ m}^2/\text{sr}$ and $6.952 \times 10^{-34}\text{ m}^2/\text{sr}$ for nitrogen and water vapor, respectively. In our analysis we used the characteristic wavelengths $\lambda_N = 386.67\text{ nm}$, which corresponds to a Raman shift of 2330.7 cm^{-1} , and $\lambda_H = 407.52\text{ nm}$, which corresponds to a Raman shift of 3654.0 cm^{-1} . As indicated by Eq. (10) the convolved function, $\langle \sigma_X | \varepsilon_X \rangle$, is the calculated differential cross section (i.e., the strength of a transition) multiplied by the filter function (refer to Subsection 3.B) at the wavelength associated with the transition and integrated over $\Delta\lambda_x$. Using Eq. (11), the convolved differential cross sections at a temperature of 273.15 K were found to be, $1.294 \times 10^{-34}\text{ m}^2/\text{sr}$ and $2.775 \times 10^{-34}\text{ m}^2/\text{sr}$ for nitrogen and water vapor, respectively.

The dominant error in these numbers is due to uncertainties in the cross sections. Following Penney and Lapp [13], we assume an error of 10% in the ratio of these cross sections. Therefore, $(d\sigma_N(\pi)/d\Omega)/(d\sigma_H(\pi)/d\Omega) = 0.395 \pm 0.039$ and $\langle \sigma_N | \varepsilon_N \rangle / \langle \sigma_H | \varepsilon_H \rangle = 0.466 \pm 0.047$. Graphed results for the convolved differential cross-section calculations are shown in Fig. 4. The values of $F(T)$, which give the temperature dependence of the convolved differential cross section are also shown for a temperature range of 200–320 K.

D. Mapping Experiment

The equipment for the mapping experiment is shown in Fig. 5. A dual-axis translation system was used. The translation system was located inside the laboratory about 1 m above the telescope's primary mirror and about 1 m below the exit/entrance windows that are used to allow operations of the lidar

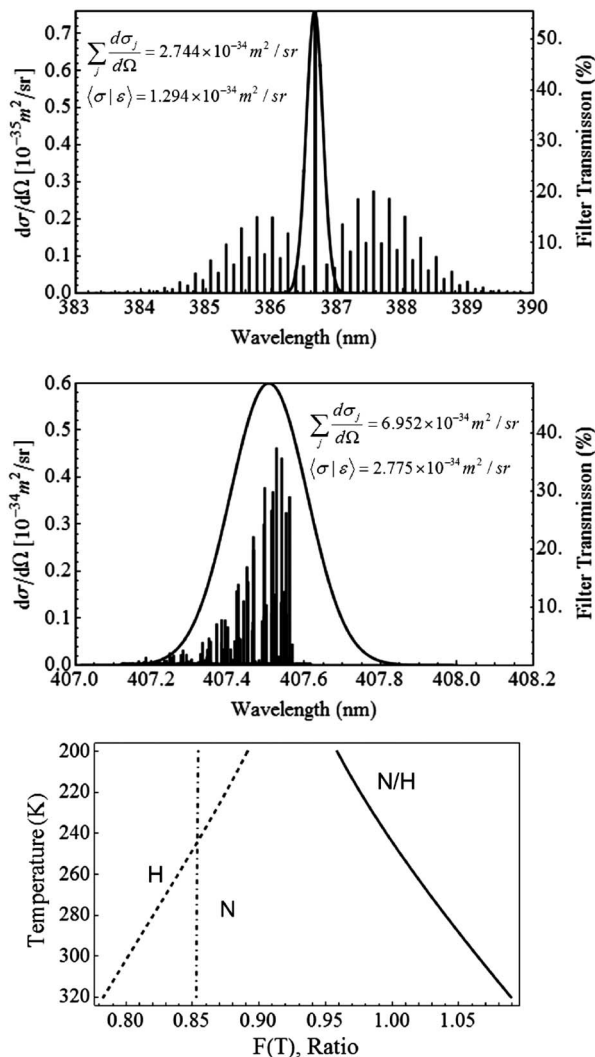


Fig. 4. Spectra of vibrational-rotational transitions at $T = 273.15$ K, associated with Raman scattering for nitrogen and water vapor. The excitation wavelength is 354.7 nm. The Q-branch vibrational transition for the nitrogen case (represented by the black vertical line) has been scaled down for graphical purposes. Also shown are the respective filter functions. The values of $F(T)$ are also shown in the lower graph.

in moderately inclement weather. The dual-axis translation system consists of two Newport Corporation Model M-IMS600 High Performance Long-Travel Linear Stages (Newport Corporation, USA), with submillimeter resolution and accuracy.

The dual-axes stage allowed the lamp to be moved to any position above the aperture of the telescope. Data were collected at each lamp position (or data cell) at a repetition rate of 30 shots per second for ~ 300 shots. Each detector accumulated data for 0.8 ms per shot. These parameters were set to match normal lidar operations for the system and resulted in $\sim 10^6$ counts accumulated per cell per channel for the 200 W lamp. The lamp filament was approximately 10 mm long by 5 mm wide and was oriented in the x - y plane with its axis angled at 45° to both the x and y axes of the scan pattern. The 45° orientation

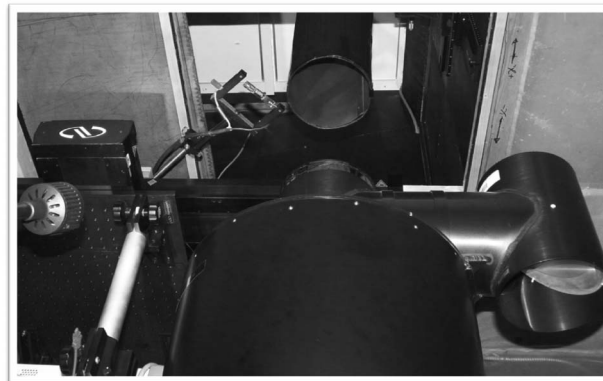


Fig. 5. Experimental setup for the mapping apparatus. The lamp is approximately 1 m above the primary mirror and about 1 m below the system exit/entrance windows. The translation stages are Newport Corporation Model M-IMS600 High Performance Long-Travel Linear Stages, with submillimeter resolution and accuracy. This picture shows the lamp in a typical scan configuration located above the telescope-secondary-periscope system and below the exit baffle.

was designed to compensate for the geometry of the lamp by providing uniform illumination at each lamp position for equal increments in both the x and y directions. Typical two-dimensional (2D) maps of $S_{HN,i}^{out}$ were obtained under these conditions.

The effect of the entrance window (Starphire, Sterling Glass, Ltd., UK) was found by placing the lamp in the roof hatch above the window and taking the ratio $S_{HN,i}^{out}$ at a single location for cases with and without the window in place. The correction factor was found to be 1.015 ± 0.004 . All data taken with this onroof configuration were collected at night to minimize background light effects.

Because of obscurations (such as the telescope supports, the optical fiber cable, the edges of the mirrors, and any debris on the primary mirror surface) on the telescope, as shown in Fig. 6A, invalid data cells existed and needed to be eliminated accordingly. The invalid (or obstructed) data cells could be distinguished from the valid (or unobstructed) data cells, since the unobstructed regions had different reflectivity, hence different values for $S_{HN,i}^{out}$ from the regions with obscurations. Obstructed data cells were eliminated by superimposing a software data mask over the $S_{X,i}^{out}$ data. The software data mask was implemented using the 355 nm channel by scanning through the recorded data of this channel for the maximum value and values below 50% of the maximum. Data cells corresponding to values below 50% of the maximum were tagged as the obstructed cells and were eliminated from the individual data sets for the nitrogen and water vapor channels. This data mask proved to be effective in eliminating cells that contain various obscurations. A representation of a typical scan is shown in Fig. 6. A resolution of $10 \text{ mm} \times 10 \text{ mm}$ was used in the scan shown. To determine the optimal scan resolution, data were first taken using scans with 10 mm resolution. These data were analyzed, and it was determined that there

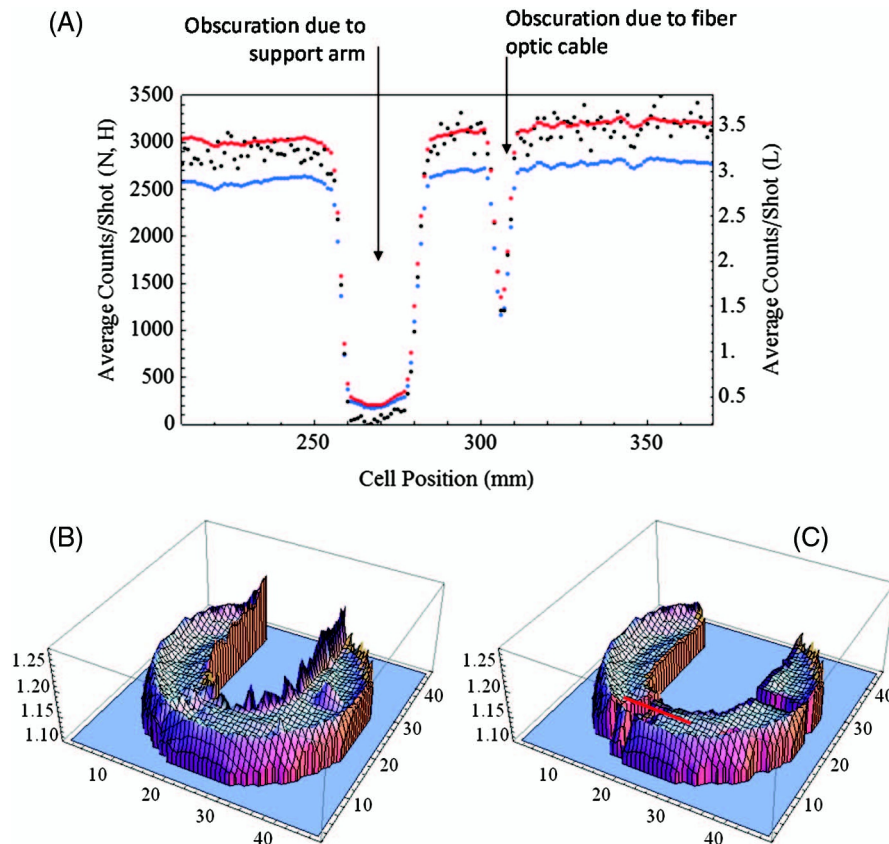


Fig. 6. (A) Plot of the mapped data for a linear scan over a portion of the telescope for the water vapor (H, red dots), nitrogen (N, blue dots), and aerosol backscatter (L, black dots) channels. The drop-offs in the data are due to reduced reflectivity from obscurations in the telescope. 2D representations of a full mapping scan (B) before and (C) after the data mask has been applied. The obscurations and mirror edges cause higher efficiency ratios for the affected cells (B). The data-mask removes these values from the analysis. The thick red line at the bottom left in (C) shows the approximate location of the linear scan shown in (A).

were no significant differences in the mean and standard deviation when analyzing the same data set at 10 mm or 20 mm resolution. For the 2D scan shown in Fig. 6, S_{HN}^{out} was found to be 1.157 ± 0.013 . When the same data set was analyzed at 20 mm resolution, S_{HN}^{out} was determined to be 1.157 ± 0.012 . However, at a lower resolution (40 mm) it was observed that the standard deviation in the analyzed points increased to as high as 0.04. It was therefore decided to use a resolution of 20 mm for data collection to minimize the time required for a full scan (about 0.5 h for a 20 mm \times 20 mm resolution scan) as well as to provide adequate precision.

To test the reliability of the measurements for S_{HN}^{out} , we investigated the repeatability (1) when measuring only a single cell over a short time frame, and (2) when scanning over multiple cells for an extended period of time. Results, as shown in Fig. 7, for the first case are presented as a histogram of 120 individual measurements of $S_{HN,i}^{\text{out}}$ in a single cell without repositioning the x - y stage. The average value for these measurements was 1.153 ± 0.002 . The relatively small standard deviation for these measurements (a relative error of about 0.17%) is indicative of the high precision of these measurements. A similar test was conducted whereby $S_{HN,i}^{\text{out}}$ was

measured in a single cell when the x - y stage was repositioned after each measurement. A total of 25 measurements were made. The stage was moved by 100 mm in both the x and the y directions and then moved back to the original location between each reading. The relative error for these measurements was 0.17%, which again indicates the high precision of the measurements even with stage repositioning. For the second case, repeatability of measurements over individual cells for an extended period of time was performed by using data from 14 full scans over the time period of September 2009 through April 2010. A total of 207 cells were evaluated (i.e., a value of $S_{HN,i}^{\text{out}}$ was calculated for each cell) and an ensemble average for each cell was obtained. Additionally, a relative error was obtained by dividing the difference in the maximum and minimum of the 14 values for a given cell (referred to as the extreme difference) by the mean for those 14 values. A histogram of the relative errors, with respect to the average value of $S_{HN,i}^{\text{out}}$ of the 14 measurements for each cell, is shown in Fig. 7. The histogram includes all 207 cells. The relative error of the extreme differences with respect to the mean value is found to be approximately 1.3%.

For these experiments, the change in the overall system efficiency factor was 1%–2% when considering

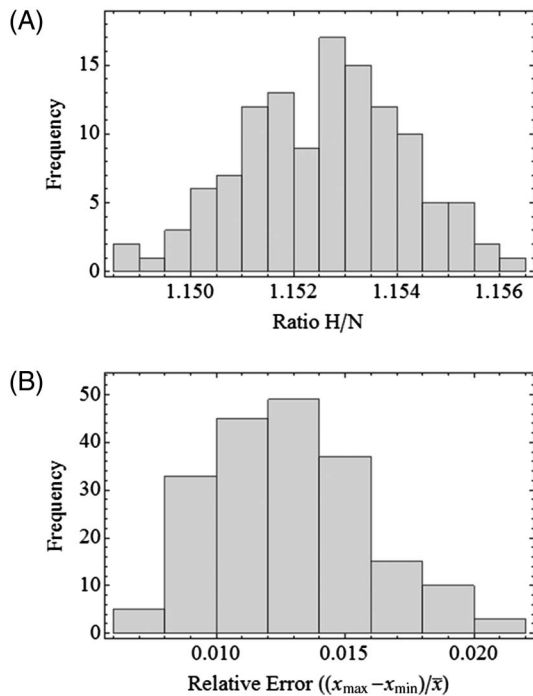


Fig. 7. (A) Histogram of the ratio of the measured signals in the water vapor channel to the measured signal in the nitrogen channel for 120 repeated measurements at a single location over the telescope mirror. The mean for the case shown was 1.153 ± 0.002 . (B) Histogram of the relative errors in the extreme differences for 14 scans taken between September 2009 and April 2010. A total of 207 cells were evaluated for each of the 14 scans. The mean relative error in the extreme differences was 1.28%.

an individual cell. This indicates that the use of a single lamp location for monitoring variations in the calibration factor, as proposed by Leblanc and McDermid [2], would have provided stability at the 1%–2% level for this set of experiments. However, as discussed previously [3], measurements in an individual cell represent just a small part of the optical system; therefore care should be taken in using single cell measurements for determining overall lidar optical efficiency.

During the summer of 2010, HURL participated in a summer measurement campaign that involved taking both daytime and nighttime data (see Subsection 3.E). It was observed that the average value of S_{HN}^{out} for data obtained for the summer of 2010 was $\sim 2\%$ less than the value obtained during the fall/winter of 2009/2010. These changes could be due to small perturbations of the system (for example, slight movement of optical components, cleaning of the primary, etc.) that might have occurred during the preparation of the system for the summer campaign.

E. Determination of C_R

During the time period June 2010 through August 2010, HURL participated in an extensive measurement campaign at the Beltsville Research Facility. During this time period, we conducted 10 full map scans of the telescope. The average value of S_{HN}^{out}

for these scans was determined to be 1.131 ± 0.011 . Correcting this value for the effects of the Starphire entrance window, using the average value given above for S_{HN}^{in} , and using the parameters given in Fig. 3 to calculate $\varepsilon(\lambda) \equiv \mathcal{F}_{\text{Gauss}}(\lambda)$, the ratio $S_{HN}^{\text{in}}/S_{HN}^{\text{out}}$ was found to be 0.857 ± 0.014 . The time-independent value of the water vapor mixing ratio calibration factor, C_R , calculated from Eq. (8), was thus found to be $187.8 \pm 18.8 \text{ g/kg}$. During this same time period, 25 radiosondes (Vaisala RS92, Vaisala, Finland) were launched from a collocated sight at the facility. Lidar data were also obtained during each of these soundings. Radiosondes were launched both day and night and under a variety of weather conditions. The mean of the ratios of the water vapor mixing ratio obtained from the radiosonde data and the lidar data, $P(\lambda_H, z)/P(\lambda_N, z)$, was determined. A typical example is shown in Fig. 8 for the radiosonde launched on July 24, 2010, at 0656 UT. The lidar data were corrected for $F(T)$. The data were averaged to 5 min temporal resolution and 30 m spatial resolution; and were corrected for differential transmission as previously described [7]. The mean ratio was determined for an altitude range of 0.5 to 1.5 km. For our system at altitudes above 0.4 km, the ratio of the overlap functions for the water vapor and nitrogen channels is essentially 1.0 [7]. A value for the mean ratio of $195.8 \pm 8.7 \text{ g/kg}$ was determined, and this value is defined to be the water vapor mixing ratio

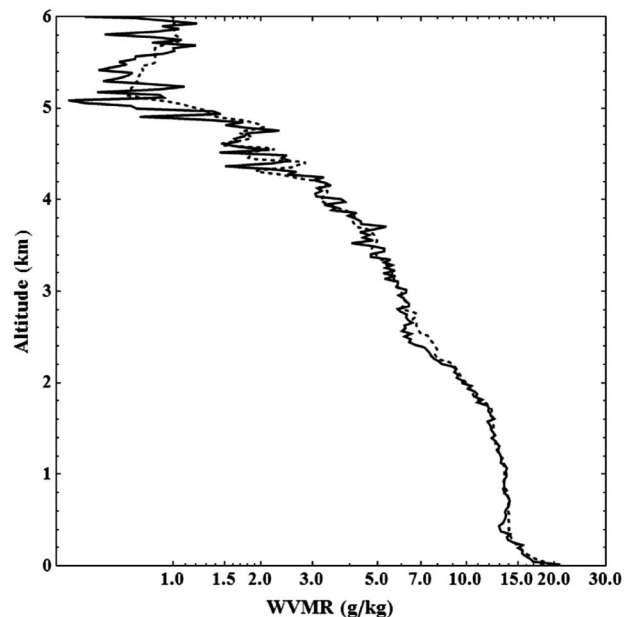


Fig. 8. Plot of lidar data (solid curve), i.e., ratio of water vapor channel to nitrogen channel signals and data from a collocated Vaisala RS92 radiosonde (dashed curve) for July 24, 2010 at 0656 UT. The lidar data shown have 5 min temporal resolution and 30 m spatial resolution. The calibration constant obtained using the radiosonde data was $195.2 \pm 3.0 \text{ g/kg}$ for the case shown. The lidar data were corrected for $F(T)$ and for differential transmission as discussed by Adam *et al.* [7], and the calibration constant was obtained for data between 0.5 and 1.5 km. The average value for all cases in this study was $195.8 \pm 8.7 \text{ g/kg}$.

calibration factor determined from radiosonde measurements. This value is in good agreement (within 5%) with the value of C_R determined from the mapping experiment.

It is instructive to investigate the temperature-dependent form of the water vapor mixing ratio calibration term, as given by Eq. (9), to determine the range of errors that could be anticipated if the lidar data were not properly corrected for $F(T)$. The graph in Fig. 9 shows that C'_R can range from ~ 180 to ~ 200 g/kg for atmospheric temperatures ranging from 200 to 300 K. A comparison of these values to C_R of 187.8 ± 18.8 g/kg that we obtained results in errors ranging from about -4.2% to 6.5% . If lidar data are not corrected for $F(T)$, the water vapor mixing ratio calibration factor would have to be treated as a variable of temperature and hence of altitude. Under this scenario, a variable value of $C'_R(T(z))$ must be applied to the lidar data to obtain a properly calibrated profile for $w(z)$. Since this approach would be undesirable, we recommend calculation of the temperature correction factor, $F(T)$, and applying it to the lidar data.

F. Sensitivity Analysis

In general, considerable effort is required to obtain accurate data to characterize the shapes of the narrowband filters. As a final part of this paper, we investigate the sensitivity of C_R to the filter parameters, such as filter baseline offset, central wavelength (λ_0), and FWHM bandwidth. The filter parameters were defined in Fig. 3. The results of these analyses are presented in Figs. 10–12.

C_R is dependent on changes in any baseline offset in the filters. Baseline offsets—additive increases in the transmission at each wavelength within the bandpass of the filters—have been investigated and the results are shown in Fig. 10. Baseline offsets were restricted to less than 1.0% transmission for these analyses. It is assumed that such values represent typical errors in the ability to measure the baseline (the zero offset) of individual interference filters. Analysis shows that C_R changes approximately linearly as the baseline offset increases. C_R changes in

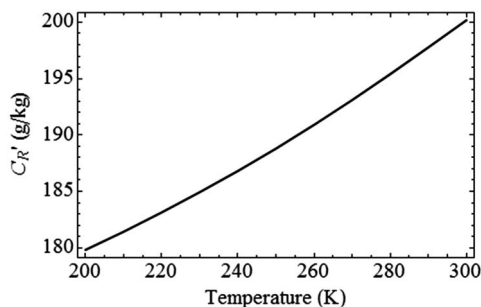


Fig. 9. Graph of the temperature-dependent form of the water vapor mixing ratio calibration factor (C'_R) versus temperature. The curve allows the calculation of the error in the temperature-independent form of the water vapor mixing ratio calibration factor (C_R) when the $F(T)$ correction is not applied to the lidar data.

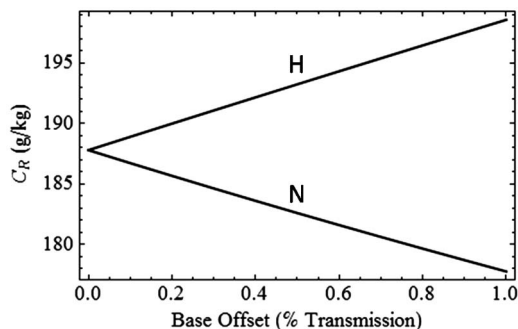


Fig. 10. Graphical representation of the change in C_R as a function of baseline offset for a temperature of 273.15 K. The plot corresponds to an additive increase in the transmission at each wavelength within the bandpass of the filter. The additive term is the value of the baseline offset in percentage points.

the positive direction for baseline increases in the water vapor filter. The rate of change is approximately 10 g/kg per 1% baseline increase. C_R changes in the negative direction for changes in the nitrogen filter baseline. For this case, the rate of change is approximately -10 g/kg per 1% baseline increase.

The water vapor mixing ratio calibration factor determined using the method described in this paper is dependent on the central wavelength of the transmission filter, λ_0 . The variations in C_R due to changes in λ_0 were investigated for each filter. Results are shown in Fig. 11. The shapes of the response curves are indicative of the change in transmission of the filter at the characteristic wavelength λ_X as λ_0 is varied. In practice, this is manifested as a mismatch between the peak filter transmission and

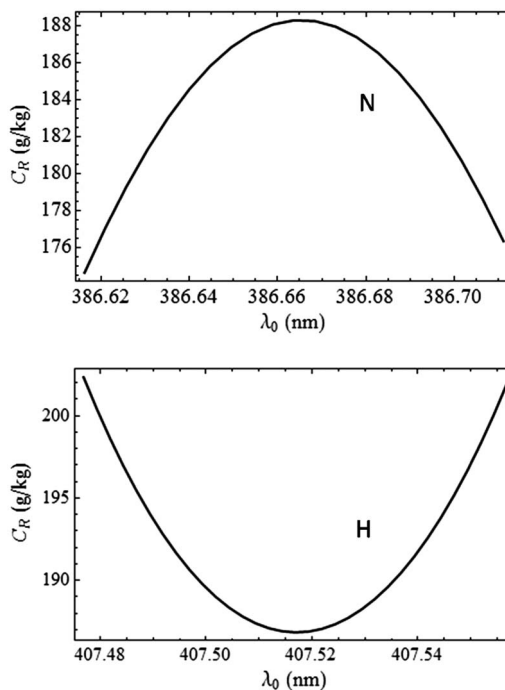


Fig. 11. C_R as a function of the filter's central wavelength, λ_0 , for the nitrogen filter and the water vapor filter at a temperature of 273.15 K.

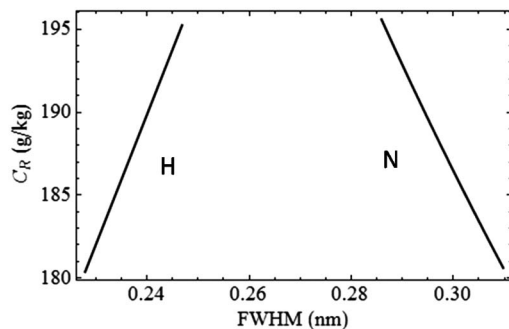


Fig. 12. C_R as a function of the filter's FWHM for the nitrogen and water vapor filters at a temperature of 273.15 K.

the wavelength band of the Raman emission. A small error in the determination of λ_0 results in significant error in C_R . For example, an absolute error of 0.05 nm in λ_0 results in a relative change as large as 10% (or ~ 19 g/kg) in C_R . The change in C_R error grows rapidly with increasing error in the determination of λ_0 —an absolute error of 0.1 nm results in a relative error of as much as 31% in C_R . For the water vapor filter, an absolute error of 0.05 nm in the determination of λ_0 results in a relative error of about -19% (~ 36 g/kg) in C_R . For larger errors in λ_0 , an absolute error of 0.1 nm results in a relative error of about 80% (or ~ 150 g/kg) in C_R .

The use of narrowband-pass filters is essential for achieving acceptable signal-to-noise ratios in systems that make daytime water vapor measurements in non-solar-blind spectral regions. When using the calibration technique we have described in this paper, errors in the determination of the FWHM of these narrowband filters lead to errors in the determination of C_R . Figure 12 gives a graphical representation of the values found for C_R as a function of the FWHM of the interference filter. These results are restricted to wavelengths within a few tenths of a nanometer of the nominal values for our filters (0.30 nm for nitrogen and 0.24 nm for water vapor). These results indicate errors in C_R of about -63 g/kg per 0.1 nm for the nitrogen filter and about 78 g/kg per 0.1 nm for the water vapor filter.

The findings discussed above suggest that considerable care must be taken in determining the inter-

ference filter characteristics when investigating the water vapor mixing ratio calibration factor. Table 1 presents information on the sensitivity of the calibration constant to changes in interference filter parameters. What is given is the magnitude of change in each of the baseline offset, the central wavelength, and the FWHM of the interference filters needed to yield a change in C_R of 3%. These can be considered as limiting accuracies for constraining the calibration constant.

4. Summary and Conclusions

In this paper we have investigated a technique that allows for the direct calculation of the water vapor mixing ratio calibration factor for a Raman lidar system that uses narrow bandwidth interference filters. Using data obtained at the Howard University Beltsville campus during the summer of 2010, a water vapor mixing ratio calibration factor for HURL was obtained from 10 mapping scans and compared to the mean calibration factor obtained by direct comparison of 25 simultaneous lidar and radiosonde profiles. The former value of the water vapor mixing ratio calibration factor was found to be 187.8 ± 18.8 g/kg and is in good agreement with the latter value of 195.8 ± 8.7 g/kg. The sondes used were Vaisala RS-92 (Vaisala, Finland) radiosondes. The radiosonde-based calibration factor was determined by a mean ratio of lidar and radiosonde data in the lower troposphere. These radiosondes have a documented wet bias in the lower troposphere of approximately 3%–4% [14] that has not been corrected for in these comparisons. Correction for this wet bias in the radiosondes should lead to even better agreement between the calibration factors obtained from the map results and from the radiosonde comparisons.

Our results indicate that a direct determination of the water vapor mixing ratio calibration factor for Raman lidar systems can be achieved when the characteristics of the interference filters are known with sufficient accuracy and a calibrated lamp mapping technique is used to determine the relative efficiencies of the lidar water vapor and nitrogen signal channels. We have shown that the results are quite sensitive to the accuracy to which we know the required filter parameters (FWHM, central wavelength, and baseline offset). Upper limits of uncertainty in these filter parameters were provided to constrain the uncertainty in the derived lidar calibration to 3% or less (exclusive of any errors in the ratio of the cross sections). Our experience is that filter specifications from the vendor (Materion Barr Precision Optics and Thin Film Coatings, USA) typically meet these accuracy requirements.

A calibration lamp used in a fixed position in front of the telescope has been proposed as a way to transfer a radiosonde-based calibration, determined during intensive campaigns, forward in time without the routine use of radiosondes. This technique, referred to as the hybrid technique [2], is attractive due to the elimination of the need to launch radiosondes

Table 1. Upper Limits on the Uncertainties in Individual HURL Filter Parameters Permissible to Constrain the Relative Uncertainty in C_R to 3% or Less^a

Filter	Baseline Offset (absolute offset)	Central Wavelength (relative difference, nm)	FWHM (relative difference, nm)
Nitrogen	$\sim 0.5\%$	$\sim 0.009\%$ (0.02 nm)	$\sim 3\%$ (0.01 nm)
Water vapor	$\sim 0.5\%$	$\sim 0.006\%$ (0.02 nm)	$\sim 3\%$ (0.009 nm)

^aIf each of the six parameters were uncertain by the values in the table, and if the uncertainties are considered to be independent, the total uncertainty in C_R would be approximately 7% or $(\sum_1^6 0.03^2)^{1/2}$.

for extended periods of time. The map results presented here indicate that the single-cell efficiency ratios agreed with the overall system efficiency to within 1%–2%. This supports the use of the hybrid technique. However, a lamp at a fixed position in front of a telescope receiver samples just a small fraction of the telescope aperture and could provide spurious results if a small contamination occurred on the telescope directly in front of the lamp [3]. For this reason, we recommend the use of multiple lamps in fixed positions to implement the hybrid technique, instead of just a single lamp, in situations where mapping is not practical.

In considering a calibration technique to use for long-term monitoring of water vapor, it is attractive for that measurement to be independently calibrated from first principles. The technique demonstrated here meets that objective. The first principles calibration relies on the knowledge of the water vapor to nitrogen cross section ratio, the uncertainty of which was assessed to be $\pm 10\%$ [13]. However, there are two pieces of empirical information that point to the possibility that the uncertainty in this cross section ratio may actually be less than the stated 10%. The first is the agreement within $\sim 5\%$ of the calibration values determined from the map calibration results presented here and the radiosonde-based technique. The second is the agreement to within 8% of the *ab initio* calculations of the cross section performed by Avila *et al.* [9] and those of Penney and Lapp [13].

Although determining the calibration of the Raman lidar system from first principles using the mapping procedure is more labor-intensive than other techniques, it is attractive due to its independence from any external measurement of water vapor. If in the future the knowledge of the Raman cross section ratio is improved, correction of past data from a lidar that has been calibrated from first principles can be performed by a simple multiplicative correction. A first principles technique, where the optical efficiency of the Raman water vapor lidar is regularly quantified, would therefore appear to be an attractive technique for meeting the calibration requirements for generating a climate quality water vapor time series. It should be pointed out, however, that small error sources such as signal-induced noise or fluorescence can influence upper altitude measurements of the water vapor mixing ratio [1–3]. Neither the first principles nor the operational radiosonde-based calibration techniques discussed here would reliably detect small errors due to these contaminants. Careful quality control of the lidar data will be required to guard against such effects.

This research was supported in part by National Aeronautics and Space Administration (NASA) Cooperative Agreements NNX07AF22 and NNX08BA42 and National Oceanic and Atmospheric Administration (NOAA) Cooperative Agreement NA06OAR4810172.

References

1. V. Sherlock, A. Hauchecome, and J. Lenoble, "Methodology for the independent calibration of Raman backscatter water vapor lidar systems," *Appl. Opt.* **38**, 5816–5837 (1999).
2. T. Leblanc and I. S. McDermid, "Accuracy of Raman lidar water vapor calibration and its applicability to long-term measurements," *Appl. Opt.* **47**, 5592–5603 (2008).
3. D. N. Whiteman, D. D. Venable, and E. Landulfo, "Comments on: Accuracy of Raman lidar water vapor calibration and its applicability to long-term measurements," *Appl. Opt.* **50**, 2170–2176 (2011).
4. A. Sobral-Torres, E. Landulfo, D. Whiteman, and D. Venable, "Water vapor Raman lidar independent calibration," in *Reviewed and Revised Papers presented at the 24th International Laser Lidar Conference*, (Organizing Committee of the 24 International Laser Lidar Conference, 2008), pp. 204–207.
5. E. Landulfo, R. F. Da Costa, A. S. Torres, F. J. S. Lopes, D. N. Whiteman, and D. D. Venable, "Raman water vapor lidar calibration," *Proc. SPIE* **7479**, 74790J (2009).
6. D. D. Venable, E. Joseph, D. Whiteman, D. Belay, R. Connell, and S. Walford, "Development of the Howard University Raman lidar," Second Symposium on Laser Atmospheric Applications held at the 85th Annual Meeting of the American Meteorological Society, San Diego, California, January 2005, <http://ams.confex.com/ams/pdfpapers/85650.pdf>.
7. M. Adam, B. B. Demoz, D. N. Whiteman, D. D. Venable, E. Joseph, A. Gambacorta, J. Wei, M. W. Shephard, L. M. Miloshevich, R. L. Herman, C. D. Barnet, J. Fitzgibbon, and R. Connell, "Water vapor measurements by Howard University Raman lidar during the WAVES 2006 campaign," *J. Atmos. Ocean. Technol.* **27**, 42–60 (2010).
8. D. N. Whiteman, "Examination of the traditional Raman lidar technique. I. Evaluating the temperature-dependent lidar equations," *Appl. Opt.* **42**, 2571–2592 (2003).
9. G. Avila, J. M. Fernández, G. Tojeda, and S. Montero, "Raman spectra and cross sections of H₂O, D₂O, and HDO in the OH/OD stretching regions," *J. Mol. Spectrosc.* **228**, 38–65 (2004).
10. W. E. Schneider and D. Goebel, Standards for "Calibration of optical radiation measurement systems," in *Laser Focus, Electro-Opt.* **9**, 12–20 (1984).
11. Optronics Laboratories, 4632 36th Street, Orlando, Florida, USA (personal communication, 2009).
12. M. Adam, "Notes on temperature-dependent lidar equations," *J. Atmos. Ocean. Technol.* **26**, 1021–1039 (2009).
13. C. M. Penney and M. Lapp, "Raman-scattering cross sections for water vapor," *J. Opt. Soc. Am.* **66**, 422–425 (1976).
14. L. M. Miloshevich, H. Vomel, D. N. Whiteman, and T. Leblanc, "Accuracy assessment and correction of Vaisala RS92 radiosonde water vapor measurements," *J. Geophys. Res.* **114**, D11305 (2009).